



Insight into the effect of co-doped to the photocatalytic performance and electronic structure of g-C₃N₄ by first principle

Zhi Zhu^{a,1}, Xu Tang^{a,1}, Tianshuai Wang^{c,1}, Wenqian Fan^b, Zhi Liu^b, Chunxiang Li^a, Pengwei Huo^{a,*}, Yongsheng Yan^{a,*}

^a Institute of the Green Chemistry and Chemical Technology, School of Chemistry and Chemical Engineering, Jiangsu University, Zhenjiang 212013, PR China

^b Institute of Chemistry for Functionalized Materials, Faculty of Chemistry and Chemical Engineering, Liaoning Normal University, Dalian 116029, PR China

^c School of Materials Science and Engineering Beihang University Beijing 100191, PR China

ARTICLE INFO

Keywords:

Co-doped
Photoelectric properties
High-efficiency
Density functional theory
Photocatalytic degradation 2-mercaptobenzothiazole

ABSTRACT

Developing low-cost and high-efficiency g-C₃N₄ (CN) semiconductor with modification has been proved to possess the potential advantage for environmental remediation in recent years. Herein, element doping of CN framework was found significantly on controlling its electronic structure. The new two-dimensional photocatalyst of Co-doped CN (Co-CN) applicable in photocatalytic reactions for 2-Mercaptobenzothiazole degradation was designed and synthesized. It was for the first time revealed that the Co-N bonding could lead to enhance significantly photoelectric properties, the rate for electron-hole pairs separation and photocatalytic activity in comparison with bulk CN. The characterization and density functional theory (DFT) results insight into the reason that the 3d electrons of the doped Co has excellent contribution to adjust the band gap of Co-CN. The present work provide a broadening window for Metal-doped CN with outstanding performance.

1. Introduction

Photocatalysis technology is regarded as a promising approach for water purification and energy crisis since it utilizes solar energy [1,2]. A large number of reports about graphitic carbon nitride (g-C₃N₄) have been well investigated in water pollution and treatment due to its resistance to acid, alkali, and photocorrosion, and excellent features for band position and operatable modification [3]. Unfortunately, the g-C₃N₄ suffers from some disadvantages, such as fast recombination of photogenerated electron-hole, low efficient visible-light utilization [4,5]. Therefore, it is highly desirable and challenging to develop new strategies for constructing g-C₃N₄ based photocatalyst.

Nowadays, various strategies have been explored to solve its deficiencies of g-C₃N₄, such as combining with other semiconductors to construct composite photocatalysts, element doping and morphological modification [6–8], among which doping with other elements is a representative approach, such as the Zn [9], Ag [10], Fe [11] doped g-C₃N₄ had been built and got tremendous strides forward. On the one hand, element doping can tune the edge positions of the valence band (VB) and conduction band (CB) to generate the localized energy levels in the band structure of g-C₃N₄ system [12,13]. On the other hand, elements doping usually has the function of suppressing the

recombination rate of charge carriers as well as narrowing the band gap of g-C₃N₄ [14]. Based on those reports, it can be predicted that introducing an impurity into a two-dimensional g-C₃N₄ could overcome the two deficiencies above. Moreover, the incorporation of metal like Co into g-C₃N₄ could be a reasonable strategy due to its active chemical properties during photocatalytic reactions [15]. To the best of our knowledge, few theoretical investigations have been reported, while experimental studies have made initial attempts of Co-doped g-C₃N₄. However, the surface chemical state of the doped Co and the substitution position in g-C₃N₄ are confused. The influence on the electronic structure of g-C₃N₄ and the formation energies are still unknown. Therefore, it is critical to explore the issues mentioned above through theoretical and experimental studies, while overcoming the deficiencies of g-C₃N₄. There have been a lot of reports on theoretical calculation, and combining calculation with experiments are inevitable trend [16,17], which can be better revealed performance changes of semiconductor materials, especially in photocatalysis field.

Motivated by the above consideration, we for the first time fabricated and characterized the two-dimensional Co-doped g-C₃N₄ nanosheets by multiple calcinations and applied them to remove 2-Mercaptobenzothiazole (acting as a kind of mercaptan with specific toxicity and environmental impacts), aiming at improving the

* Corresponding authors.

E-mail addresses: huopw@mail.ujs.edu.cn (P. Huo), yys@mail.ujs.edu.cn (Y. Yan).

¹ These authors contributed equally to this work.

photocatalytic activity, determining the doped position of Co, reducing the band gap, elucidating the intrinsic reasons of the photocatalytic enhancement of g-C₃N₄. In present work, we identified the morphology, structure, specific surface area, photoelectric properties, the possible photogenerated carriers migration process and degradation mechanism, and systematically studied aforementioned critical issues of Co-doped g-C₃N₄ via the density functional theory (DFT) and experiments.

2. Experimental section

2.1. Materials

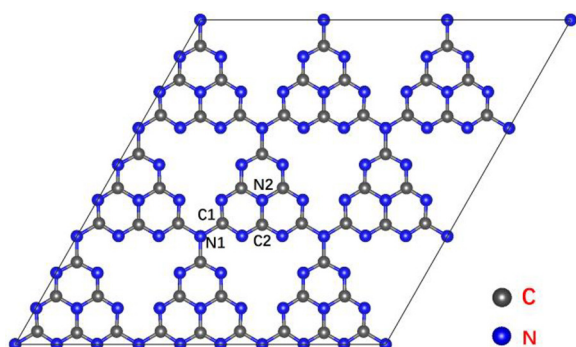
Melamine (AR), 2-Mercaptobenzothiazole (AR), NH₃H₂O solution (25.0%) and oleic acid (99%) were purchased from Aladdin Chemistry Co., Ltd., p-benzoquinone (BQ, AR), isopropanol (IPA, AR), CoCl₂·6H₂O, triethanolamine (TEOA, AR), ethanol (C₂H₅OH, AR) and 5, 5-dimethyl-L-pyrroline N-oxide (DMPO, AR) were supplied by Aladdin Chemistry Co., Ltd. Deionized water was used throughout all experiments.

2.2. Synthesis

The synthesis process of g-C₃N₄ (CN) was as follows: 3.0 g melamine was heated to 500 °C from room temperature in an open crucible and holding for 2 h. Then rising the temperature to 550 °C with a ramping rate of 2.3 °C min⁻¹ and holding for 2 h. After cooling down to room temperature, heat the milled powder at 500 °C for another 4 h with the same ramping rate. Diffusing a certain amount of CN and CoCl₂·6H₂O into 50 mL H₂O with stirring at 70 °C in a water bath for some time, then calcinate the mixture at 300 °C for 2 h to get the Co-CN. The structure of the monolayer CN in Scheme 1 shows four possible doping sites for Co atom in substitution with the N atom or C atom. The doping model is also exhibited in Fig. 11.

2.3. Computational method

Density functional theory (DFT) as implemented in the Vienna Ab initio Simulation Package (VASP) using projector augmented wave (PAW) formalism was used in the system energy and electronic structure calculations [18,19]. Perdew-Burke-Ernzerhof (PBE) in the form of Generalized gradient approximation (GGA) was used as the exchange-correlation functional [20]. The Gaussian smearing method was used [21], and the width of smearing was chosen as 0.05 eV. The energy cutoff for plane-wave expansion of the PAW's was 400 eV. The optimized lattice constant of g-C₃N₄ was 7.13 Å, according to previous computational and experimental results [22,23]. The slab model is a 3 × 3 × 1 supercell containing 54 C atoms and 72 N atoms. In the vertical direction, a vacuum layer of 17 Å in thickness is introduced for all the surfaces. The Brillouin zone is sampled using Monkhorst-Pack scheme with a k-point mesh of 3 × 3 × 1 in the Gamma-centered grids



Scheme 1. Optimized structure of monolayer g-C₃N₄. N1, N2, C1, C2 are four possible doping sites of Co.

for the structural relaxation [24], and a 9 × 9 × 1 k-point mesh for the static calculations of all the systems. The convergence criteria of maximum force for the structure relaxation was 0.03 eV/Å.

2.4. Detailed experimental process

The experimental process of photocatalytic activity test, photo-electrochemical measurements and trapping experiments are given in the supporting information.

2.5. Characterization

X-ray diffraction patterns (XRD) of samples were collected on a Thermo ESCALAB 250XI spectrometer, with a scanning speed of 7° min⁻¹. The X-ray photoelectron spectroscopy (XPS) measurements were conducted by Thermo ESCALAB 250X (America) electron spectrometer using 150WAl Kα radiations. Transmission electron microscopy (TEM) images were obtained by F20S-TWIN electron microscope (Tecnai G2, FEI Co.). The scanning electron microscopy (SEM) and energy dispersive X-ray spectroscopy (EDS) were characterized by a field emission scanning electron microscopy (JSM-7800 F, Japan). Fourier transform infrared (FT-IR) spectra were collected on Nicolet Magna-IR 550 spectrometer within the wavelength range of 400–4000 cm⁻¹. The N₂ adsorption-desorption and Brunauer-Emmett-Teller (BET) method and porosity analyzer (NDVA-2000e). The Ultraviolet visible diffused reflectance spectra (UV-vis DRS) were obtained via a UV-vis spectrophotometer (A Shimadzu UV-3600) using BaSO₄ as the reference. The photoluminescence spectra (PL) were obtained on F4500 photoluminescence detector (Hitachi, Japan). Atomic force microscope (AFM, MFP-3D, U.S.) was used to observe the thickness of samples. Transient photocurrent, electrochemical impedance spectroscopy (EIS) were performed in the electrochemical workstation (Zahner Instruments, Germany). Electron spin resonance (ESR) was carried on electron paramagnetic resonance spectrometer (A300-10/12, Bruker).

3. Result and discussion

3.1. Structure and morphology characteristics

The crystalline structural characteristics of the as-prepared CN and Co-CN were analyzed by XRD measured (Fig. 1). The peaks at 13.6° and 27.3° were indexed as the (100) and (002) peaks of pristine CN could be found, which corresponded to the in-plane structural packing motif of tri-s-triazine units, agreed well with the PDF no. 50-1250 data [25]. Interestingly, the peak at 13.6° and 27.3° almost appeared in Co-CN, but

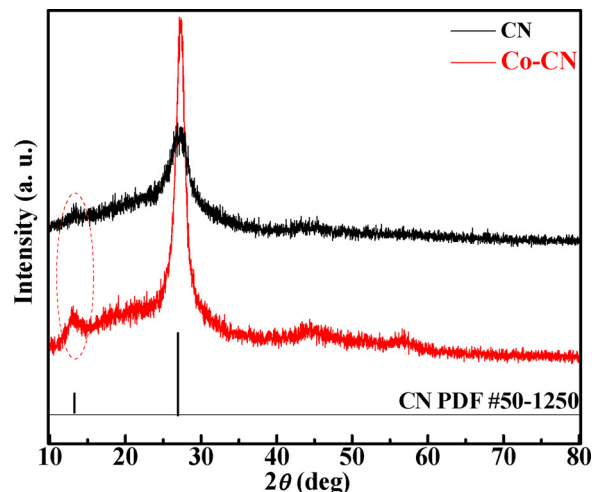


Fig. 1. XRD patterns of CN and Co-CN.

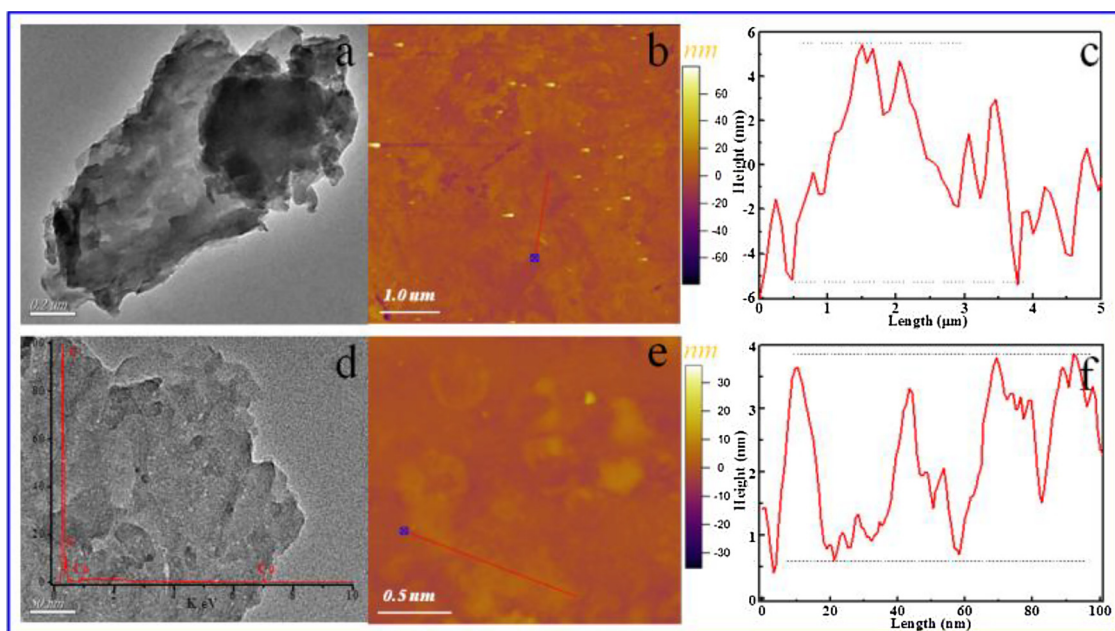


Fig. 2. Typical TEM images (a, d), AFM image (b, e) and height profile along the line in AFM (c, f) of CN and Co-CN. The EDX single of Co-CN in insert curve (d).

these peaks become sharper and obvious, it meant that the crystallinity and structure of Co-CN was enhanced. The changing must originate from the interaction of CN and Co. So that, the results illustrated that the Co might be doped into CN sheets and it was enough to imply that Co-CN was successfully synthesized.

TEM and AFM analysis observed the morphologies of as-prepared CN and Co-CN. It can be seen that the CN showed an agglomerated structure, an obviously large size with several micrometers (Fig. 2a), and the thickness is more than approximately 11 nm (Fig. 2b–c). Moreover, the as-synthesized samples from CN to Co-CN displayed the typical sheet-like architectures, the thickness recorded by AFM is approximate 3 nm, as shown in Fig. 2e–f. It means that the doped Co may adjust the thickness and band gap of CN. Meanwhile, using EDX spectroscopy analyses of Co-CN sample (the inset of Fig. 2d), the Co, C and N elements are detected out, without any O element single, which indicates the Co species may be doped in CN instead of formation oxide and accordance with the XRD result. Moreover, the SEM images of CN to Co-CN showed in Figure S1 can also observed the surface information and thickness. Therefore, the TEM and AFM measurement further prove that the Co-CN has two-dimensional sheet structure.

Three-dimensional structure and roughness of the synthesized samples are shown in Fig. 3. The roughness of CN ($R_b = 5.784$) is much higher than that of Co-CN ($R_b = 1.360$) from the three-dimensional images and the calculated data for roughness. The results reveal that after doping, the Co-CN displays typical nanosheets architectures with a smooth surface and small sheet thickness, which are coincident with the results of the obtained AFM images. We analyzed that the decreasing roughness may reduce the transmission resistance of electron and enhance the photocatalytic activity. Also, the different roughness would affect the specific surface area of the samples, as the nitrogen adsorption/desorption isotherm is employed and shown in Figure S2. The samples exhibit type-IV characteristic isotherm curves with H1 hysteresis loops in the mesoporous materials [26]. The pore size distributions of 16 nm for CN and 29 nm for Co-CN testify mesoporous properties. Moreover, the specific surface area of bulk CN was calculated to be $20.3 \text{ m}^2 \text{ g}^{-1}$, and that of Co-CN decreased to $1.2 \text{ m}^2 \text{ g}^{-1}$. It is a possible that the specific surface area of different samples may vary with the roughness. In general, the high specific surface area might improve the photocatalytic activity of photocatalyst due to high adsorption ability of photocatalysts [27–29]. In present work, however,

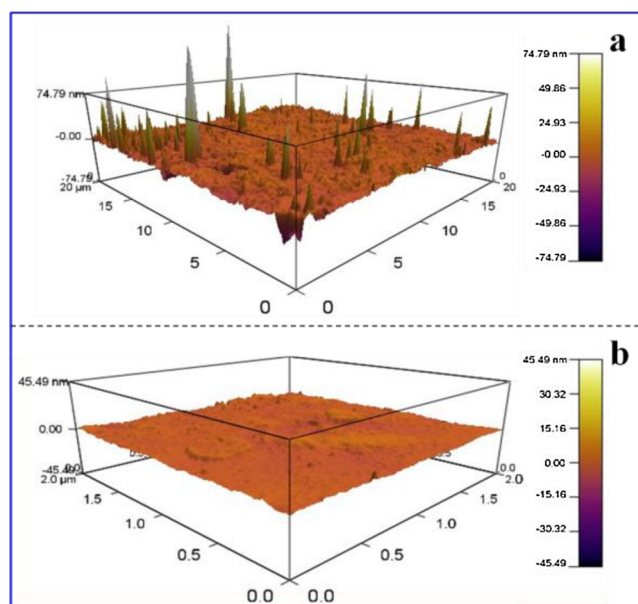


Fig. 3. Three-dimensional models of CN (a) and Co-CN (b) draw from AFM images.

the photocatalytic activity of CN is lower than that of Co-CN (Fig. 7a), and the critical, influential factors to the photocatalytic activities are optical and electrical properties rather than BET surface areas.

3.2. Surface chemical composition and functional group analysis

The FT-IR and Raman spectra of the synthesized samples are shown in Fig. 4A. For CN, the sharp peak at 808 cm^{-1} is the characteristics vibration for the out-of-plane bending of triazine rings. The absorption bands in the region of $1200 - 1650 \text{ cm}^{-1}$ (1241 , 1318 , 1425 and 1635 cm^{-1}) are attributed to the typical stretching modes of C–N and C=N heterocycles [30,31]. The broad peaks at around $3100 - 3400 \text{ cm}^{-1}$ can be assigned to N–H and O–H vibratio from the surface uncondensed amine groups and absorbed water molecules [32]. Interestingly, the Co-CN resembles the characteristic bands of CN, the

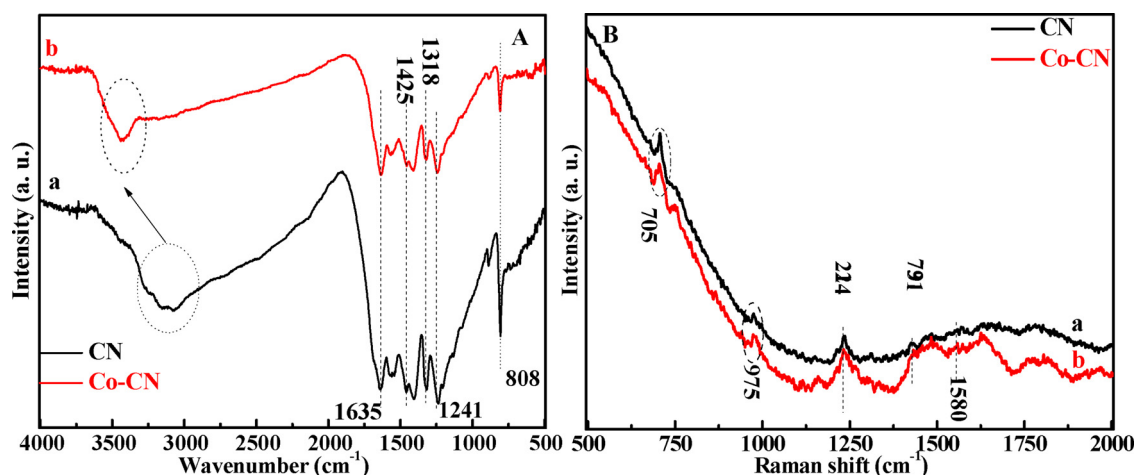


Fig. 4. FT-IR spectra (Left) and Raman spectra (Right) of CN (a) and Co-CN (b).

typical graphitic structure of carbon nitride are well reserved after homogeneous Co doping. However, the peak around $3100\text{--}3400\text{ cm}^{-1}$ is much narrower and stronger than that of CN. Additionally, the sharp band at 808 cm^{-1} are weakened, and more uncondensed amino groups and hydroxyl are dropped off or replaced. The conjugated structures of C–N are stretched and a highly conjugated system forms. The reason might arise from the introduced Co that establishes a surface chemical bonding through the Co–N formation and causes the charge transfer between Co and CN [33].

In the Raman spectra (Fig. 4B), the peaks located at 705 cm^{-1} , 974 cm^{-1} and 1234 cm^{-1} stem from the vibration modes of C–N heterocycles in both compounds. Two peaks observed at 1379 cm^{-1} and 1580 cm^{-1} correspond to the D band and G band of the graphite-like structures [34]. Interestingly, compared with the CN, these peaks aforementioned in Co-CN are much broader and stronger. In general, the enhanced Raman intensity may result from the electromagnetic interaction, coupling or metal doping [35]. On the one hand, it indicates that the Co-doped in CN made the ordered graphitic structure stronger and structural defect become weaker. On the other hand, Raman enhancement factors could be attributed to the charge transfer between Co and CN molecules [36], the Raman spectra are consistent with the FT-IR results. Moreover, the charge transfer is also studied by differential charge density (Fig. 13).

The surface chemical states of Co-CN were investigated by XPS. The deconvoluted peak centered at 284.4, 286.2 and 288.6 eV in the C 1s spectra (Fig. 5a) can be attributed to the C–C, hydroxylated surface carbon atoms (C–OH) and CN_3 [37], correspondingly. Fig. 5b displays the typical heptazine repeating units with several N species at different binding energies, the three peaks at 398.4, 400.1 and 404.0 eV can be assigned to triazine rings (C–N=C), tertiary nitrogen ($\text{N}(\text{C})_3$) groups and amino functions (N–H) [38], respectively. In comparison with the binding energy of metallic Co ($\sim 779\text{ eV}$), the dominant peak in Fig. 5c

at $\sim 781.2\text{ eV}$ (Co $2p_{3/2}$) ascribes the Co (II) state in the form of Co – N. The binding energy at 797.1 eV is in good agreement of Co $2p_{1/2}$ and the peak at 785.1 eV is due to the satellite shake-up peaks of the assigned components. Thus, the Co was successfully doped into CN excluding the presence of cobalt oxide and metallic Co in the composites [39,40].

3.3. Optical properties analysis

UV–vis diffuse reflectance spectroscopy for the synthesized samples are shown in Fig. 6. The absorption edges of CN is around 450 nm (Fig. 6a), while the absorption edge of the Co-CN possesses red-shifted in comparison with bulk CN. More importantly, the optical absorption intensity of Co-CN was significantly enhanced at the range of 550–650 nm. The results can describe the Co doping effect that makes a secondary absorption to the visible light, and it would promote the spread of visible light and absorption efficiency in the system, resulting in a higher photocatalytic activity [41]. To further study the effect of doped Co on optical band gap energy of Co-CN, the Kubelka-Munk method was used to calculate the band gap of the prepared samples [42]. In Fig. 6b, the optical band gap energy was calculated by the plots of $(\alpha h\nu)^2$ versus $h\nu$, and that CN and Co-CN are 2.70 eV and 2.55 eV, respectively. Moreover, the CB potential was further investigated by XPS valence band analysis as shown in Fig. 12. Therefore, the doped Co can effectively regulate the band gap and broaden absorption range of CN for visible light.

3.4. Photocatalytic behaviors and recyclability test

We studied the influence of different contents cobalt doses on the degradation 2-Mercaptobenzothiazole (Figure S3). The optimum is 81% when the cobalt source is 0.01 g. The degradation curves means that the

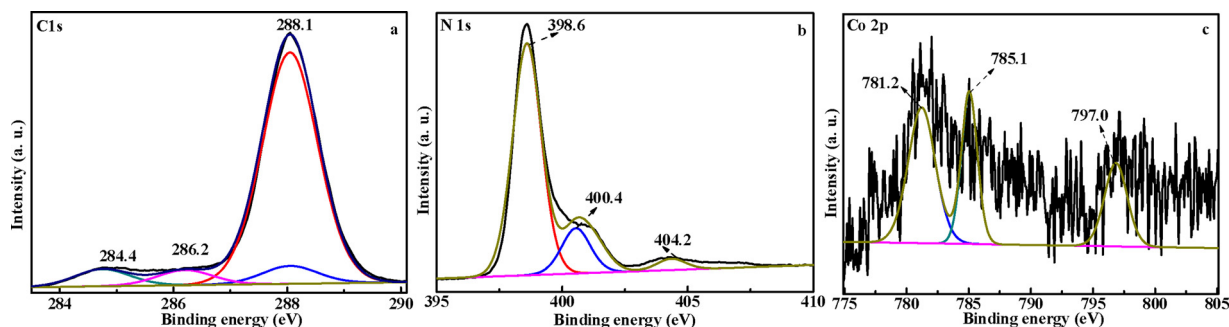


Fig. 5. XPS spectra of C 1s (a), N 1s (b), and Co 2p (c).

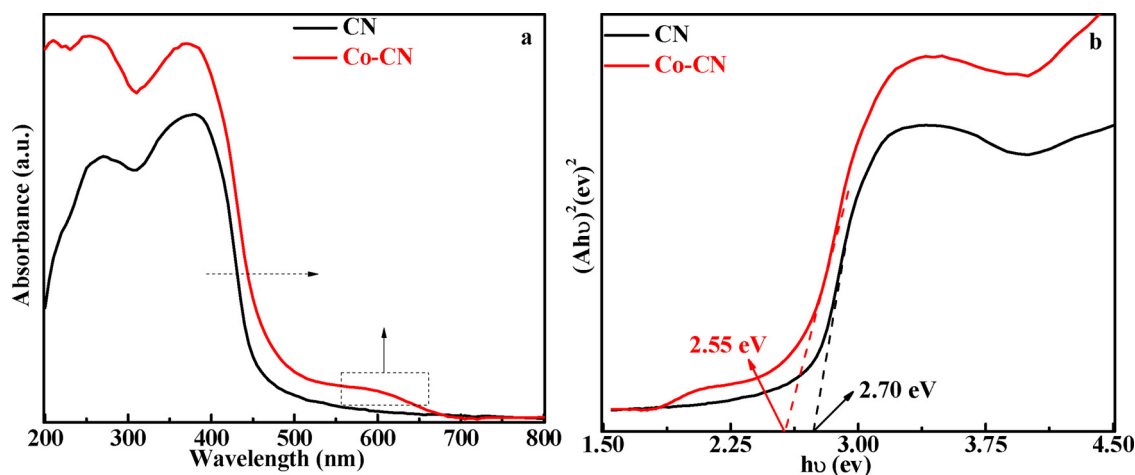


Fig. 6. The UV-vis diffuse reflectance spectroscopy (a), estimation of band gap energy (b) of CN and Co-CN.

higher or lower content of Co cannot find adequate to adjust the best energy level of CN, leading to lower light absorption and removal efficiency. The degradation and kinetics curves are depicted in Fig. 7a–b. The degradation rates are 39% and 81%, and the constant rate is 0.006 min^{-1} and 0.016 min^{-1} for CN and Co-CN, respectively. The result demonstrates that the Co-doped CN can effectively increase the separation rate of photogenerated carriers and enhance the mineralizing ability of Co-CN.

The absorbance of 2-Mercaptobenzothiazole decrease naturally along with increasing irradiation time (Fig. 7c), and the result indirectly

proved that 2-Mercaptobenzothiazole molecules were destroyed and decomposed completely. The reusability of the photocatalyst is essential for practical applications. The photocatalytic activity of Co-CN towards 2-Mercaptobenzothiazole degradation hardly reduced after recycling five runs (Fig. 7d). The degradation rate is maintained at 79%; it suggests that the Co-CN possess superior stability and good photocatalytic performance during the degradation process.

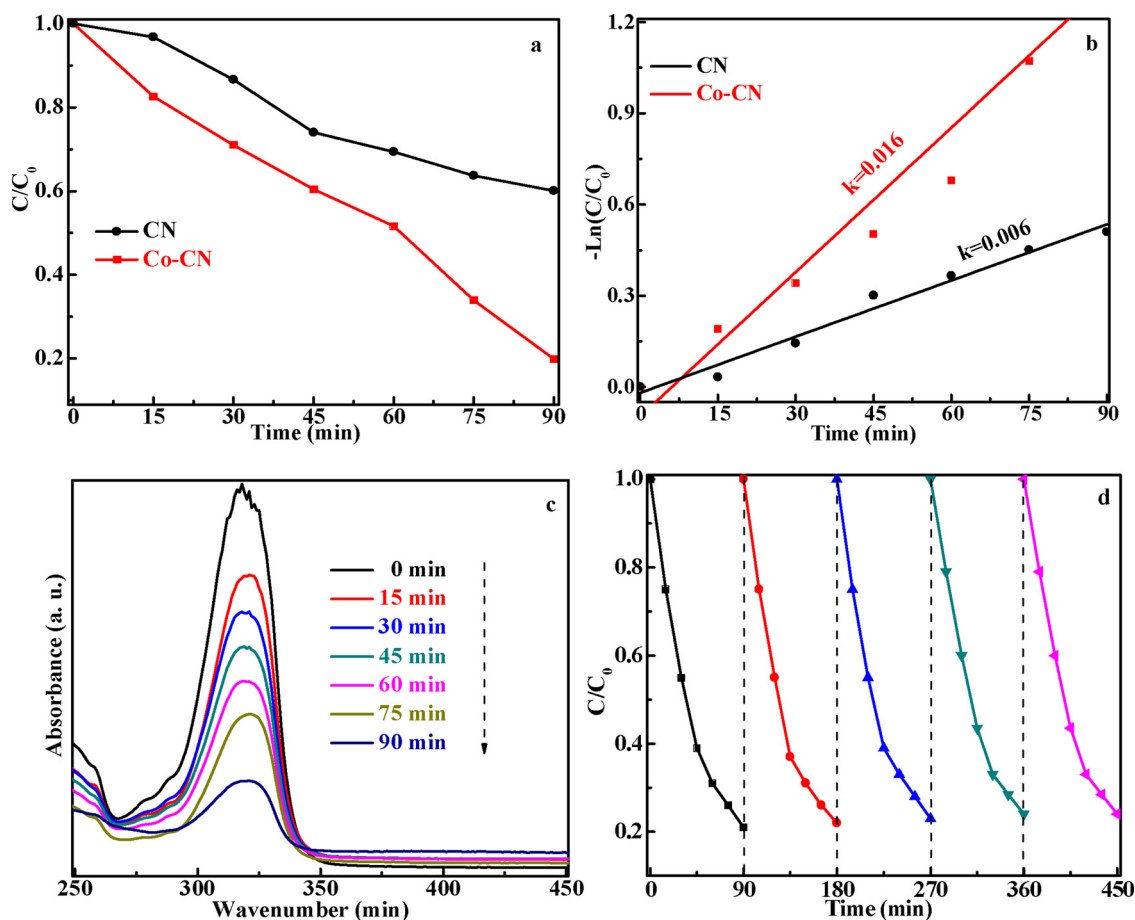


Fig. 7. Degradation dynamics curves (a) and the first-order reaction kinetics curves (b) over CN and Co-CN, the changes of UV-vis spectra of 2-Mercaptobenzothiazole (c) and cycle runs (d) degrading over Co-CN.

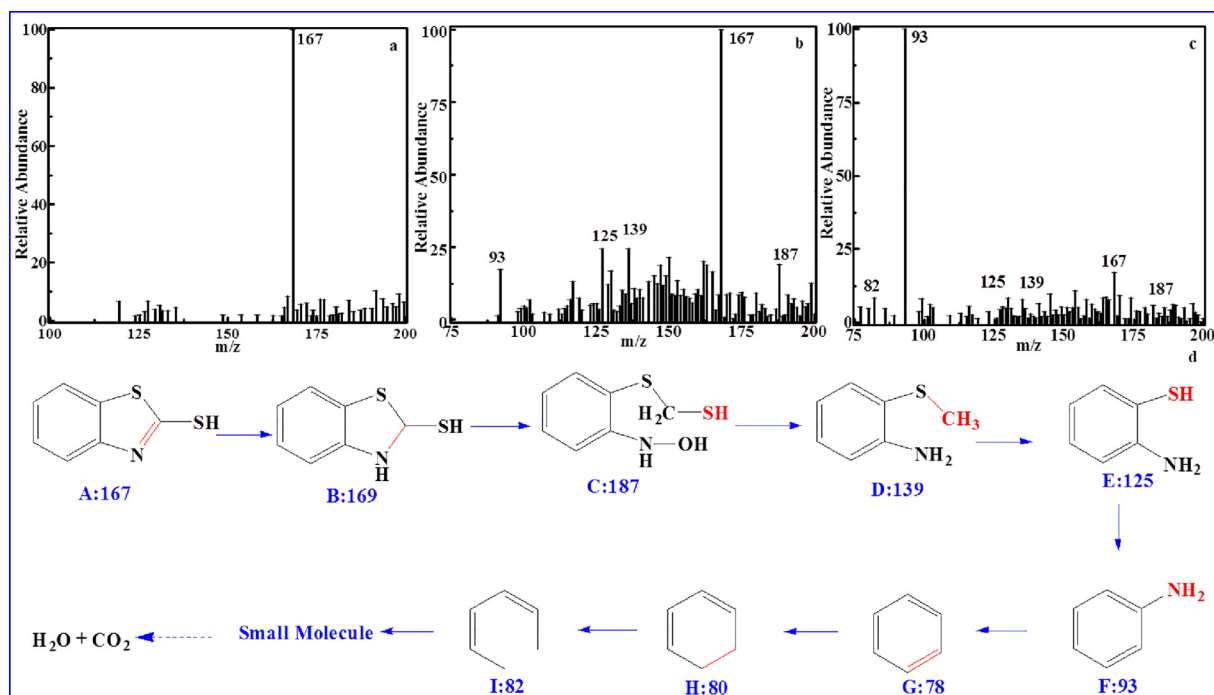


Fig. 8. m/z of degrading 2-Mercaptobenzothiazole over Co-CN: initial solution (a), degradation in 45 min (b) and degradation in 90 min (c), possible intermediate products on the degradation of 2-Mercaptobenzothiazole (d).

3.5. Intermediates and mineralization ability test

Taking into account the intermediates during the degradation process, the HPLC-MS experiments were carried out. In comparison with Fig. 8a, the peak of 2-Mercaptobenzothiazole ($m/z = 167$) decreased natural and almost disappeared after 90 min, and other peaks increased gradually (Fig. 8b-c). These results proved that 2-Mercaptobenzothiazole was decomposed into small molecules, CO_2 or H_2O [43]. According to the change of the measured mass, the possible intermediate products and the relative ions fragmentation were analyzed, the proposed degradation products and reaction pathways of 2-Mercaptobenzothiazole are shown in Fig. 8d.

3.6. Photo-electricity analysis

To gain more profound insights into the charge transport behavior of the as-prepared samples, and the PL spectrums emission at 469 nm are presented in Fig. 9. The PL peak intensity of Co-CN reduces obviously compared to that of CN (Fig. 9a). It is well-known that the lower PL spectroscopy indirectly reflects the lower recombination degree of photogenerated carriers [44], so that the Co-CN will show higher photocatalytic properties. To further verify the effect of the doped Co to the charges transfer ability in the prepared samples, the photocurrent-

time measurement was carried out [45]. The photocurrent intensity for Co-CN is nearly two times as high as that of CN (Fig. 9b); it suggests more efficient separation of electron-hole pairs in Co-CN. Therefore, the separation rate of the electrons and holes could be increased. So that, the photocurrent response gives further evidence to support the doped Co and the two-dimensional structure can promote separation of the photo-generated carriers. Meanwhile, the EIS measurement was also carried out to explore the process of the charge transfer resistance (Fig. 9c). The smaller radius of the Nyquist circle means the lower charge-transfer resistance [46]. Comparing the arc radius, the Co-CN shows a considerably smaller radius than that of bulk CN. These results coherently demonstrate Co-doped two-dimensional CN sheet has better photoelectric properties, which could promote the charge carriers separation during degradation process.

3.7. Photocatalytic mechanism

To further determine the predominant reactive species during the Co-CN degradation process, the trapping experiments were carried out (Fig. 10 a-b). When the TEOA and BQ are injected into the solution for trapping h^+ and $\cdot\text{O}_2^-$ [47], the degradation activity is serious inhibited. Moreover, the photocatalytic efficiency is also inhibited when used IPA as trapping agent to trap $\cdot\text{OH}$. Hence, the results of trapping experiment

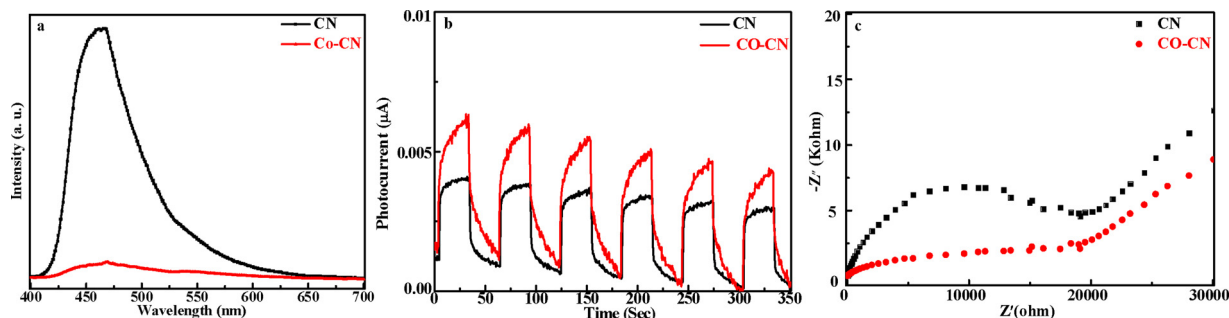


Fig. 9. PL spectra (a), transient photocurrent responses spectra (b), electrochemical impedance spectra (c) of CN and Co-CN.

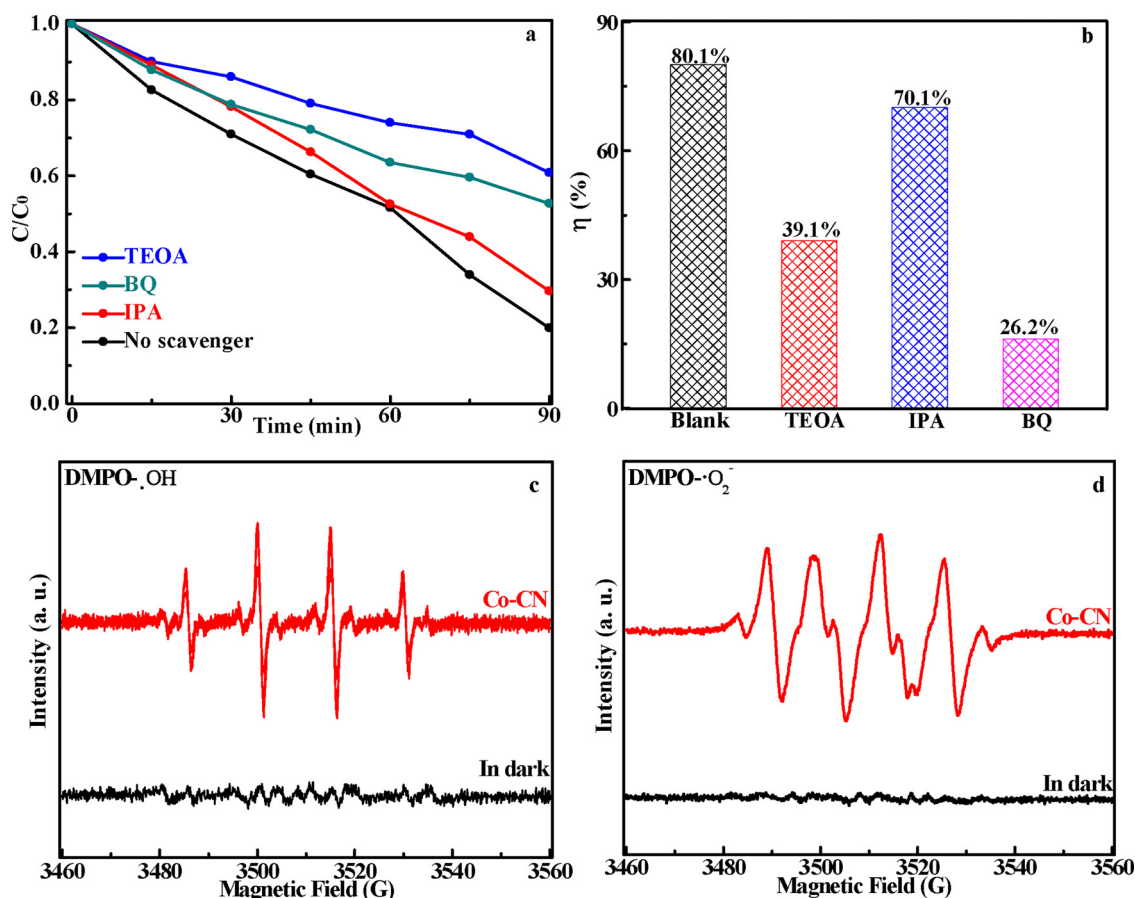


Fig. 10. The trapping experiments for degradation of 2-Mercaptobenzothiazole over Co-CN (a–b), ESR spectra of DMPO·OH and DMPO·O₂⁻ for Co-CN (c–d).

suggested that the $\cdot\text{O}_2^-$, h^+ , and $\cdot\text{OH}$ are all dominant reactive species on degradation of 2-Mercaptobenzothiazole. In addition, the reactive species were also investigated by ESR technique. It can be seen that there are no ESR signals in the dark. Interestingly, the four characteristic signals corresponding to the DMPO·OH are observed under visible light irradiation (Fig. 10c), the $\cdot\text{OH}$ may generate by the electron reacts with O_2 and H^+ in the solution [48]. It is worth mentioning that the six characteristic peaks of $\cdot\text{O}_2^-$ can be observed in Fig. 10d, indicates that the $\cdot\text{O}_2^-$ can generated in Co-CN during the degradation process. To sum up, the ESR results are consistent with trapping experiment for

active species and the $\cdot\text{O}_2^-$, h^+ and $\cdot\text{OH}$ are present in Co-CN system.

The defect formation energies (E_f) were calculated to investigate the most stable doping site, using the following equations:

$$E_f = E(\text{Co-CN}) - E(\text{CN}) - \mu(\text{Co}) + \mu(\text{N atom or C atom}) \quad (1)$$

$$4\mu(\text{N}) + 3\mu(\text{C}) = \mu(\text{CN}) \quad (2)$$

The $\mu(\text{Co})$ is obtained by $\mu(\text{Co}) = \mu(\text{Metal-Co}_2)/2$. The $\mu(\text{N})$ is defined as $\mu(\text{N}) = \mu(\text{N}_2)/2$ and the $\mu(\text{C})$ is obtained from the equations (Eq. (2)). By definitions, the system with the lowest formation energy in

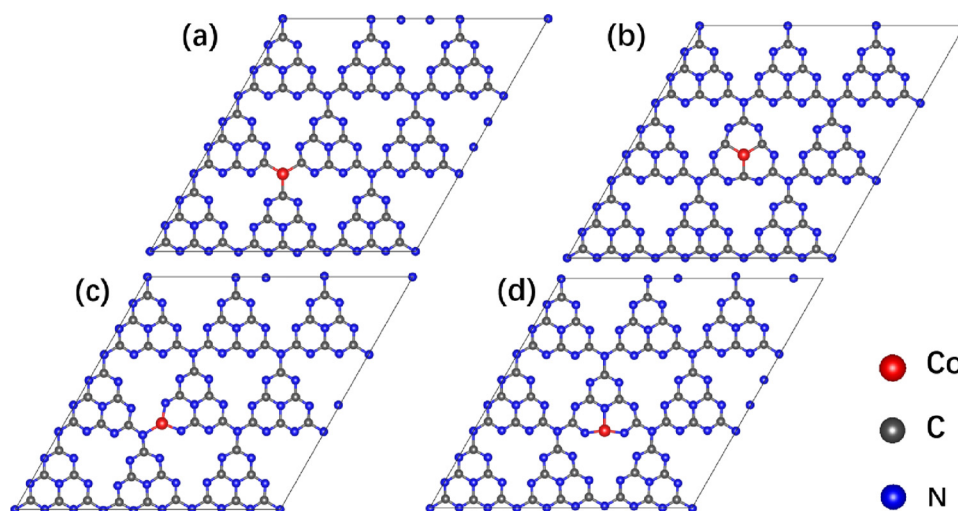


Fig. 11. Optimized structure of Co-doped CN systems with various doping sites: (a–b) N1, N2 and (c–d) C1, C2.

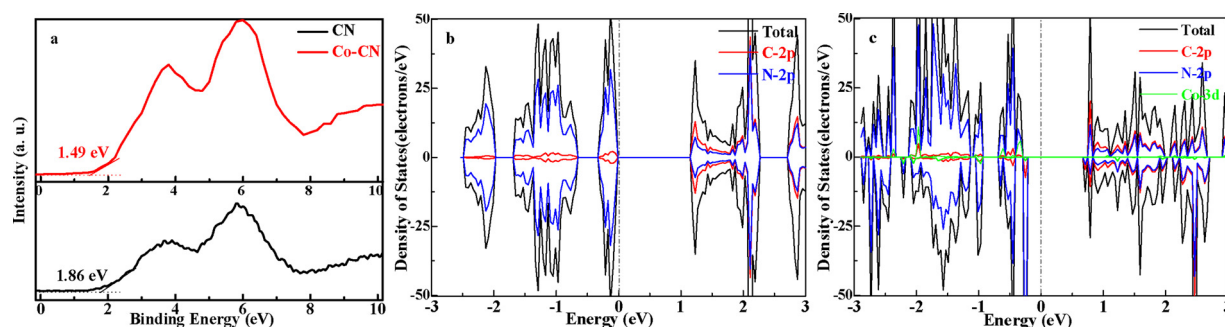


Fig. 12. XPS valence band spectra (a), the density of states (b, c) of CN and Co-CN (the dash line is the Fermi level set at zero).

Table 1

Formation energies (eV) of Co-doped monolayer CN systems with various doping sites.

Doping sites	N1	N2	C1	C2
E_f	4.34	5.63	3.28	3.49

four doping systems is the most stable in thermodynamics.

Table 1. lists the calculated formation energies of four doping systems with Co. All the formation energies are positive, which suggests that all the doping processes are endothermic and non-spontaneous thermodynamically. The results show that the formation energies of C-site doping systems are smaller than those of N site doping which means that the Co prefer to substitute the C atom sites rather than N atom sites in doping process, this result provides additional evidence of the Co-doping site revealed by FT-IR, XPS and Raman analyses.

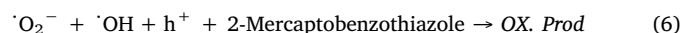
As illustrated in Fig. 12a (XPS valence band), the VB position of Co-CN (+ 1.49 eV) shifts up 0.37 eV relative to that of bulk CN (+ 1.86 eV). Thus, the CB of CN and Co-CN were calculated to be −0.84 eV and −1.06 eV, respectively, it implies that CB position of Co-CN also has up-shift 0.22 eV. The result further demonstrate that the surface Co-N bonding state decorating CN lifts up the conduction band position, which is beneficial for improving the photocatalytic degradation performance.

In order to make clear the effect of the Co-doped on the electronic structure of CN, the DOS and charge density differences of the systems were investigated, which showed in Fig. 12b–c. The band gap 1.24 eV in monolayer CN is smaller than the experimental value 2.7 eV [49], because of the well-known shortcomings (the lower exchange correlation between electrons) of the GGA functional [50]. Comparing with monolayer CN, after Co doping, the Fermi level moves to CB bottom shifting towards the longer wavelength side, and the band gap energy decreases, just as the UV–vis DRS spectra show. DOS of monolayer CN (Fig. 12b) shows that N mainly dominates the valence band, and the N and C atoms dominate the conduction band and the band gap of CN reduces to 0.96 eV after Co doping (Fig. 12c). The 3d electrons of Co atom and 2p electrons from the nearest neighboring N are hybrid within the energy range from −0.25 to −0.61 eV, indicating the strong interaction between them as the XPS analysis. After Co doping, spin up and spin down in DOS gets the symmetry breaking so that Co doping introduce the magnetic property while the monolayer CN shows non-magnetic. Therefore, the Co doping has a significant influence on the structure and band gap of CN. Moreover, the partial density of states (PDOS) of different atoms for CN and Co-CN are showed in Figures S4 and S5, we analysis the contributions changes of different atoms to the valence band and conduction band in detail.

From the above analysis, the Co has been successfully doped into the CN sheet, and it is beneficial for light absorption and band gap reduction. In order to explore the reason for band gap changes of Co-CN, we further draw out the differential charge density (Fig. 13) to directly understand the bonding and electron transfer between different

atoms. From Fig. 13, it is obvious to see that the charge density differences of the doping site area encounters a noticeable distribution change even in more distant regions. Comparing with the monolayer CN, the N atoms adjacent to the Co atoms are obtain electrons from the Co atom and then form the Co-N bonds which are consistent with the DOS analysis. We further quantified the gains and losses of the electrons between the Co atom and the three adjacent N atoms through the Bader analysis; the results show that the three N atoms gain 1.03e on average while Co atom loses 0.94e. The introduced Co causes to the charge rearrangement and reduces the band gap of Co-CN. Moreover, the charge changes (e) of the N and C atoms around the doping sites are listed in Table S1.

According to these obtained data, a tentative mechanism of photocatalytic degradation process on the Co-CN are depicted in Fig. 14. Firstly, the metal doping in Co-CN can significantly enhance the visible light absorption, which has been proven by the UV–vis and XPS valence band spectra analysis. Therefore, the Co-CN could be easily excited, and the solar energy utilization rate is improved (Eq. (3)). Secondly, due to the optimized photoelectric properties of two-dimensional Co-CN sheets, the electrons/holes could be efficiently transmitted and joining in the reaction of oxidizing reduction. The more negative CB of Co-CN (CB, −1.06 eV) ($O_2/O_2^{\cdot -}$, −0.33 eV, NHE), which can reduce O_2 to yield $O_2^{\cdot -}$ (Eq. (4)). Meanwhile, the electrons will react with O_2 and H^+ in the solution and generate $\cdot OH$ (Eq. (5)). The h^+ generated from the VB of CN could also directly oxidize the 2-Mercaptobenzothiazole (Eq. (6)), gradually destroyed during the reaction process.



4. Conclusions

In summary, the Co-doped CN (Co-CN) was successfully prepared using multiple calcinations technology. The best removal efficiency (81%) of Co-CN on degrading 2-Mercaptobenzothiazole (10 mg L^{-1}) is two times higher than that of pristine CN (36%), while the best degradation rate constant K is approximately three times than bulk CN. The DFT calculations and experimental results are both identified that the Co-doped could broaden the harvest range of visible light, narrow the band gap, increase light absorption, and drastically enhance degradation performance of CN. Therefore, the chemical doping strategy demonstrated to be highly useful to improve the photoelectric properties and provide valuable information for further development of novel photocatalytic systems and for environmental domains.

Acknowledgment

This work is financially supported by the National Natural Science

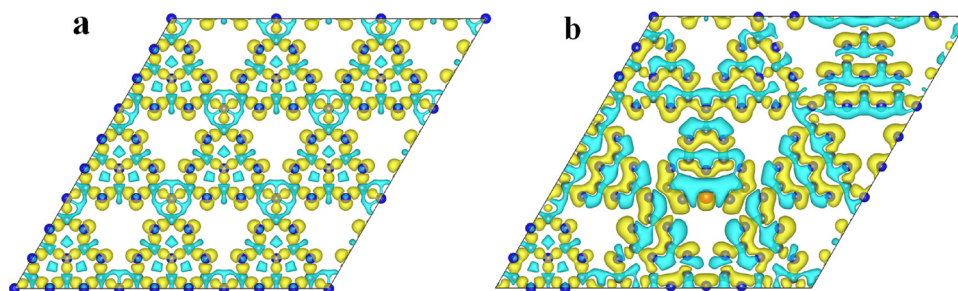


Fig. 13. Charge density difference of monolayer CN and Co-CN, blue and yellow represent the charge loss and accumulation, respectively (the isosurface value is set to 0.015e/A³) (For interpretation of the references to colour in this figure legend, the reader is referred to the web version of this article).

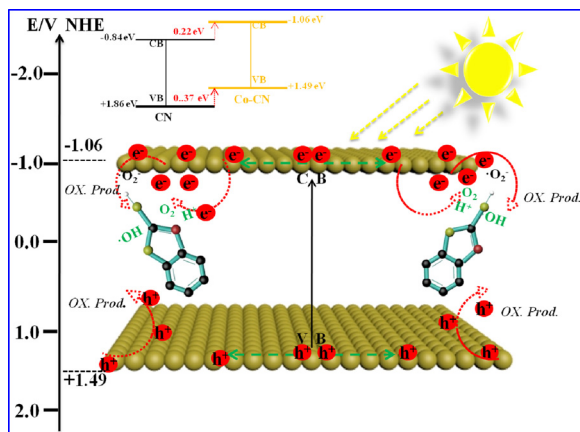


Fig. 14. Schematic illustration of the possible photocatalytic process in the Co-CN under visible light irradiation.

Foundation of China (No. U1662125, 21546013 and 21606114), the Natural Science Foundation of Jiangsu Province (No. BK20150536), China Postdoctoral Science Foundation Funded Project (No. 2015M571683, 2016M590418), also thanks to density functional theory supported of Beihang University.

Appendix A. Supplementary data

Supplementary material related to this article can be found, in the online version, at doi:<https://doi.org/10.1016/j.apcatb.2018.09.009>.

References

- [1] F. Wang, P. Chen, Y. Feng, Z. Xie, Y. Liu, Kun. Yao, W. Lv, G. Liu, Facile synthesis of N-doped carbon dots/g-C₃N₄ photocatalyst with enhanced visible-light photocatalytic activity for the degradation of indomethacin, *Appl. Catal. B* 207 (2017) 103–113.
- [2] H. Huang, R. Cao, S. Yu, K. Xu, W. Hao, Y. Wang, Single-unit-cell layer established Bi₂WO₆ 3D hierarchical architectures efficient adsorption photocatalysis and dye-sensitized photoelectrochemical performance, *Appl. Catal. B* 219 (2017) 526–537.
- [3] Z. Zhu, W. Fan, Z. Liu, H. Dong, Y. Yan, P. Huo, Construction of an attapulgite intercalated mesoporous g-C₃N₄ with enhanced photocatalytic activity for antibiotic degradation, *J. Photoch. Photobiol. A* 359 (2018) 102–110.
- [4] Y. Hong, C. Li, Z. Fang, B. Luo, W. Shi, Rational synthesis of ultrathin graphitic carbon nitride nanosheets for efficient photocatalytic hydrogen evolution, *Carbon* 121 (2017) 463–471.
- [5] R. Fei, L. Yang, Strain-engineering the anisotropic electrical conductance of few-layer black phosphorus, *Nano Lett.* 14 (2014) 2884–2889.
- [6] D. Tang, G. Zhang, Fabrication of AgFeO₂/g-C₃N₄ nanocatalyst with enhanced and stable photocatalytic performance, *Appl. Surf. Sci.* 391 (2017) 415–422.
- [7] K. Wang, G. Zhang, J. Li, Y. Li, X. Wu, 0D/2D Z-scheme heterojunctions of bismuth tantalate quantum dots/ultrathin g-C₃N₄ nanosheets for highly efficient visible light photocatalytic degradation of antibiotics, *ACS Appl. Mater. Interfaces* 9 (2017) 43704–43715.
- [8] Y. Li, X. Wu, J. Li, K. Wang, G. Zhang, Z-scheme g-C₃N₄/Cs₂WO₃ heterostructure as smart window coating for UV isolating, Vis penetrating, NIR shielding and full spectrum photocatalytic decomposing VOCs, *Appl. Catal. B* 229 (2018) 218–226.
- [9] C. Chang, Y. Fu, M. Hu, C. Wang, G. Shan, L. Zhu, Photodegradation of bisphenol A by highly stable palladium-doped mesoporous graphite carbon nitride (Pd/mpg-C₃N₄) under simulated solar light irradiation, *Appl. Catal. B* 142 (2013) 553–560.
- [10] S.W. Hu, L.W. Yang, Y. Tian, X.L. Wei, J.W. Ding, J.X. Zhong, Simultaneous nanostructure and heterojunction engineering of graphitic carbon nitride via in situ Ag doping for enhanced photoelectrochemical activity, *Appl. Catal. B* 163 (2015) 611–622.
- [11] S. Tonda, S. Kumar, S. Kandula, V. Shanker, Fe-doped and -mediated graphitic carbon nitride nanosheets for enhanced photocatalytic performance under natural sunlight, *J. Mater. Chem. A* 2 (2014) 6772–6780.
- [12] G. Liu, P. Niu, C. Sun, S.C. Smith, Z. Chen, G.Q. Lu, Unique electronic structure induced high photoreactivity of sulfur-doped graphitic C₃N₄, *J. Am. Chem. Soc.* 132 (2010) 11642–11648.
- [13] X. Ma, Y. Lv, J. Xu, Y. Liu, R. Zhang, Y. Zhu, A strategy of enhancing the photo-activity of g-C₃N₄ via doping of nonmetal elements: a first-principles study, *J. Phys. Chem. C* 116 (2012) 23485–23493.
- [14] G. Zhang, M. Zhang, X. Ye, X. Qiu, S. Lin, X. Wang, Iodine modified carbon nitride semiconductors as visible light photocatalysts for hydrogen evolution, *Adv. Mater.* 26 (2014) 805–809.
- [15] P.W. Chen, K. Li, Y.X. Yu, W.D. Zhang, Cobalt-doped graphitic carbon nitride photocatalysts with high activity for hydrogen evolution, *Appl. Surf. Sci.* 392 (2017) 608–615.
- [16] X. Lv, W. Wei, Q. Sun, F. Li, B. Huang, Y. Dai, Two-dimensional germanium monochalcogenides for photocatalytic water splitting with high carrier mobility, *Appl. Catal. B* 217 (2017) 275–284.
- [17] X. Ma, Y. Dai, L. Yu, B. Huang, Energy transfer in plasmonic photocatalytic composites, *Light Sci. Appl.* 5 (2016) e16017–e16029.
- [18] G. Kresse, J. Hafner, Ab initio molecular dynamics for liquid metals, *Phys. Rev., B Condens. Matter* 48 (1993) 13115–13118.
- [19] T. Wang, N. Zhao, C. Shi, Interface and doping effects on Li Ion Storage Behavior of Graphene/Li₂O, *J. Phys. Chem. C* 121 (2017) 19559–19566.
- [20] J.P. Perdew, J.A. Chevary, S.H. Vosko, K.A. Jackson, M.R. Pederson, D. Singh, Erratum: atoms, molecules, solids, and surfaces: applications of the generalized gradient approximation for exchange and correlation, *J. Phys. Rev. B* 46 (1992) 6671–6687.
- [21] M. Methfessel, A.T. Paxton, High-precision sampling for brillouin-zone integration in metals, *Phys. Rev. B* 40 (1989) 3616–3621.
- [22] J. Cui, S. Liang, X. Wang, Zhang, First principle modeling of oxygen-doped monolayer graphitic carbon nitride, *J. Mater. Chem. Phys.* 161 (2015) 194–200.
- [23] P. Niu, L. Zhang, G. Liu, Graphene-like carbon nitride nanosheets for improved photocatalytic activities, *Adv. Funct. Mater.* 22 (2012) 4763–4770.
- [24] S. Froyen, Brillouin-zone integration by fourier quadrature: special points for superlattice and supercell calculations, *J. Phys. Rev. B* 39 (1989) 3168–3172.
- [25] Z. Zhu, Z. Lu, D. Wang, X. Tang, Y.Y. Yan, Construction of high-dispersed Ag/Fe₃O₄/g-C₃N₄ photocatalyst by selective photo-deposition and improved photocatalytic activity, *Appl. Catal. B* 182 (2016) 115–122.
- [26] H. Che, J. Chen, K. Huang, W. Hu, H. Hu, X. Liu, Construction of SrTiO₃/Bi₂O₃ heterojunction towards to improved separation efficiency of charge carriers and photocatalytic activity under visible light, *J. Alloys. Compd.* 688 (2016) 882–890.
- [27] B. Liu, L. Liu, X. Lang, Doping high-surface-area mesoporous TiO₂ microspheres with carbonate for visible light hydrogen production, *Energy Environ. Sci.* 7 (2014) 2592–2597.
- [28] H. Che, G. Che, H. Dong, W. Hu, H. Hu, C. Liu, Fabrication of Z-scheme Bi₂O₃Cl/g-C₃N₄ 2D/2D heterojunctions with enhanced interfacial charge separation and photocatalytic degradation various organic pollutants activity, *Appl. Surf. Sci.* 455 (2018) 705–716.
- [29] J. Fu, B. Zhu, C. Jiang, B. Cheng, W. You, J. Yu, Hierarchical porous O-doped g-C₃N₄ with enhanced photocatalytic CO₂ reduction activity, *Small* 13 (2017) 1603938–1603944.
- [30] M. Gholipour, F. Bédard, T. Do, Post-calcined carbon nitride nanosheets as an efficient photocatalyst for hydrogen production under visible light irradiation, *ACS Sustain. Chem. Eng.* 5 (2017) 213–220.
- [31] Z. Sun, Q. Li, J. Hu, Q. Tang, H. Wang, Z. Wu, Enhanced CO₂ photocatalytic reduction on alkali-decorated graphitic carbon nitride, *Appl. Catal. B* 216 (2017) 146–155.
- [32] B. Lin, H. An, X. Yan, T. Zhang, J. Wei, G. Yang, Fish-scale structured g-C₃N₄ nanosheet with unusual spatial electron transfer property for high-efficiency photocatalytic hydrogen evolution, *Appl. Catal. B* 210 (2017) 173–183.
- [33] M. Vu, S. Mohan, C. Nguyen, Chemically bonded Ni co-catalyst onto the S doped g-

- C₃N₄ nanosheets and their synergistic enhancement in H₂ production under sunlight irradiation, *ACS Sustain. Chem. Eng.* 6 (2018) 4194–4203.
- [34] O. Akhavan, Graphene nanomesh by ZnO nanorod photocatalysts, *ACS Nano* 4 (2010) 4174–4180.
- [35] X. Bai, R. Zong, C. Li, D. Liu, Y. Liu, Y. Zhu, Enhancement of visible photocatalytic activity via Ag@C₃N₄ core-shell plasmonic composite, *Appl. Catal. B* 147 (2014) 82–91.
- [36] X. Ling, L. Xie, Y. Fang, H. Xu, H. Zhang, J. Kong, Can graphene be used as a substrate for Raman enhancement? *Nano Lett.* 10 (2010) 553–561.
- [37] J. Li, W. Zhao, J. Wang, S. Song, X. Wu, G. Zhang, Noble metal-free modified ultrathin carbon nitride with promoted molecular oxygen activation for photocatalytic formaldehyde oxidization and DFT study, *Appl. Surf. Sci.* 458 (2018) 59–69.
- [38] X. Zhou, L. Yang, X. Tan, G. Zhao, X. Xie, G. Du, A robust electrochemical immunosensor based on hydroxyl pillar[5]arene@AuNPs@g-C₃N₄ hybrid nanomaterial for ultrasensitive detection of prostate specific antigen, *Biosens. Bioelectron.* 112 (2018) 31–39.
- [39] M. Yuasa, A. Yamaguchi, H. Itsuki, K. Tanaka, M. Yamamoto, K. Oyaizu, Modifying carbon particles with polypyrrole for adsorption of cobalt ions as electrocatalytic site for oxygen reduction, *Chem. Mater.* 17 (2005) 4278–4281.
- [40] C. Li, Y. Du, D. Wang, S. Yin, W. Tu, Z. Chen, Unique P-Co-N surface bonding states constructed on g-C₃N₄ nanosheets for drastically enhanced photocatalytic activity of H₂ evolution, *Adv. Funct. Mater.* 27 (2017) 1604328–1604336.
- [41] W. Gao, Y. Zhao, Z. Mao, D. Bi, J. Chen, D. Wang, Enhanced visible light photocatalytic activity for g-C₃N₄/SnO₂:Sb composites induced by Sb doping, *J. Mater. Sci.* 53 (2018) 9473–9485.
- [42] M. Wang, P. Guo, Y. Zhang, C. Lv, T. Liu, T. Chai, Synthesis of hollow lantern-like Eu (III)-doped g-C₃N₄ with enhanced visible light photocatalytic performance for organic degradation, *J. Hazard. Mater.* 349 (2018) 224–233.
- [43] Z. Lu, X. Zhao, Z. Zhu, M. Song, N. Gao, Y. Wang, A novel hollow capsule-like recyclable functional ZnO/C/Fe₃O₄ endowed with three-dimensional oriented recognition ability for selectively photodegrading danofloxacin mesylate, *Catal. Sci. Technol.* 6 (2016) 6513–6524.
- [44] L. Chen, W. Ma, J. Dai, J. Zhao, C. Li, Y. Yan, Facile synthesis of highly efficient graphitic-C₃N₄/ZnFe₂O₄ heterostructures enhanced visible-light photocatalysis for spiramycin degradation, *J. Photoch. Photobio. A* 328 (2016) 24–32.
- [45] Z. Zhu, X. Tang, S. Kang, P. Huo, Constructing of the magnetic photocatalytic nanoreactor MS@FCN for cascade catalytic degrading of tetracycline, *J. Phys. Chem. C* 120 (2016) 27250–27258.
- [46] C. Li, G. Chen, J. Sun, J. Rao, Z. Han, Y. Hu, Doping effect of phosphate in Bi₂WO₆ and universal improved photocatalytic activity for removing various pollutants in water, *Appl. Catal. B* 188 (2016) 39–47.
- [47] Z. Zhu, W. Fan, Z. Liu, Y. Yu, H. Dong, Fabrication of the metal-free biochar-based graphitic carbon nitride for improved 2-Mercaptobenzothiazole degradation activity, *J. Photoch. Photobio. A* 358 (2018) 284–293.
- [48] H. Huang, X. Han, X. Li, S. Wang, P.K. Chu, Y. Zhang, Fabrication of multiple heterojunctions with tunable visible-light-active photocatalytic reactivity in BiOBr-BiOI full-range composites based on microstructure modulation and band structures, *ACS Appl. Mater. Inter.* 7 (2015) 482–492.
- [49] G. Dong, K. Zhao, L. Zhang, Carbon self-doping induced high electronic conductivity and photoreactivity of g-C₃N₄, *Chem. Commun.* 48 (2012) 6178–6180.
- [50] C. Stampfl, C. Walle, Density-functional calculations for III-V nitrides using the local-density approximation and the generalized gradient approximation, *Phys. Rev. B* 59 (1999) 5521–5535.